JPhys Energy

PAPER • OPEN ACCESS

Electronic structure and defect states in bismuth and antimony sulphides identified by energy-resolved electrochemical impedance spectroscopy

To cite this article: Daria Miliaieva *et al* 2025 *J. Phys. Energy* **7** 035012

Journal of Physics: Energy

CrossMark

OPEN ACCESS

RECEIVED
9 January 2025

REVISED
23 April 2025

ACCEPTED FOR PUBLICATION
7 May 2025

PUBLISHED
22 May 2025

PAPER

Electronic structure and defect states in bismuth and antimony sulphides identified by energy-resolved electrochemical impedance spectroscopy

Daria Miliaieva[1,*], **Vojtech Nadazdy**[2], **Mykhailo Koltsov**[1], **Cibrán López**[3,4], **Hanieh Saeeyekta**[1,5], **Jaroslav Kuliček**[6], **Claudio Cazorla**[3,4], **Edgardo Saucedo**[4,7], **Raitis Grzibovskis**[8], **Aivars Vembris**[8], **Malle Krunks**[1], **Bohuslav Rezek**[6] and **Nicolae Spalatu**[1]

[1] Department of Materials and Environmental Technology, Tallinn University of Technology, Tallinn, Estonia
[2] Institute of Physics, Slovak Academy of Sciences, Bratislava, Slovakia
[3] Departament de Física, Universitat Politecnica de Catalunya, 08034 Barcelona, Spain
[4] Barcelona Research Center in Multiscale Science and Engineering, Universitat Politècnica de Catalunya, 08019 Barcelona, Spain
[5] Department of Information Engineering, University of Padova, Padova, Italy
[6] Faculty of Electrical Engineering, Czech Technical University in Prague, Technická 2, Prague 6, Czech Republic
[7] Departament of Electronic Engineering, Universitat Politècnica de Catalunya, 08034 Barcelona, Spain
[8] Institute of Solid State Physics, University of Latvia, 8 Kengaraga str., Riga LV-1063, Latvia
[*] Author to whom any correspondence should be addressed.

E-mail: daria.miliaieva@taltech.ee

Keywords: chalcogenides, electronic structure, density of states, valence band maximum, conduction band minimum, bandgap, defects

Supplementary material for this article is available online

Abstract

One of the reasons chalcogenide-based photovoltaic solar cells (SC) do not yet meet the expected high-power conversion efficiencies is a lack of understanding of their electronic structure, and particularly the nature of the point defects in the absorber materials. We show that the density of states of the characteristic features of the electronic structure, such as band edges and energy distribution of defects, can be obtained experimentally by energy-resolved electrochemical impedance spectroscopy (ER-EIS) in a technically simple and quick way. The ER-EIS data correlate well with theoretical density functional theory calculations. The ER-EIS reveals that Bi_2S_3, has only shallow defects near the conduction band minimum (CBM). In Sb_2S_3, ER-EIS also shows deep defect states, which can be the cause of the low electrical conductivity of Sb_2S_3 and lower than theoretically possible power conversion efficiency of Sb_2S_3-based SC. A dominant sulphur vacancy defect was identified in Bi- and Sb-chalcogenides. In the $(Sb_xBi_{(1-x)})_2S_3$ ternary alloy series, a gradual transformation of CBM and defect states in the band gap was observed. Notably, a 1:9 ratio of Bi:Sb cations already transforms the deep sulphur defects into shallow ones while keeping the band edges similar to those of the pristine Sb_2S_3. It can provide a novel strategy for healing the deep defect states in Sb_2S_3, a crucial step for boosting solar cell performance.

1. Introduction

Chalcogenide (Ch) semiconductors, owing to their high absorption coefficient, are particularly attractive for thin-film (TF) solar cells (SC) as sustainable and low-cost alternatives to traditional silicon-based PV technologies. Copper indium gallium selenide (CIGS) absorbers and CdTe, which have been on the market for over two decades, so far have achieved a certified power conversion efficiency (PCE) of 23.6% and 23.1%, respectively, as shown in the NREL chart [1]. However, national regulations and scarcity of the constituent elements motivated further research for new types of TF SC. One of the approaches was substituting scarce In^{3+}/Ga^{3+} in CIGS with Zn^{2+} and Sn^{4+} [2] to get Cu_2ZnSnS_4 (kesterite or CZTS). $Cu_2ZnSn(S,Se)_4$ or CZTSSe, a derivative of CZTS, remained for a decade at PCE of 12.6% reached in 2014 [3]. Only in 2024, the PCE jumped to a promising 14.9% [4] due to understanding the nature of the defects in the absorber and

choosing the correct defect passivation strategies. In addition to defects, the narrow phase stability window facilitates the secondary crystallographic phase formation during CZTSSe (and CZTS) growth and post-growth processes [5], contributing to SC performance deterioration.

Therefore, the emerging class of post-transition metals with lone ns^2 pair in electron configuration (Pb^{2+}, Sn^{2+}, Ge^{2+}, Sb^{3+}, and Bi^{3+}) were proposed as defect-tolerant semiconductors [6]. These materials have ribbon-like crystal structures with covalent bonds inside the ribbon and van der Waals bonds in between the ribbons (so-called pseudo-1D structure). Due to the flexibility of van der Waals bonds, pseudo-1D chalcogenides are reported to self-heal the defects at the grain boundaries by forming new intra- and inter-ribbon bonds [7]. At the same time, special post-treatment processes (such as chloride and alkali treatments) are required to heal the grain boundary defects in established CdTe and CIGS TFs [8]. Moreover, pseudo-1D Chs were reported to have a single stable crystallographic phase [8–10].

Compounds of Sb^{3+} and Bi^{3+} are set apart from the rest of pseudo-1D materials not only by ecological friendliness and earth abundance but especially by a high absorption coefficient ($\sim 10^5$ cm^{-1}). Another speciality of Sb^{3+} and Bi^{3+} chalcogenides is the absorption coefficient near the band edge, which is significantly higher than in other Ch materials, including CIGS and CZTS. It enables the prospect of ultrathin (<100 nm) photoabsorbers that have advantages not only in material saving, light weight, and flexibility of the final device but also in efficient photogenerated carrier extraction due to a higher fraction of the space charge region compared to thicker absorbers [8].

The Bi_2S_3 bandgap of 1.2–1.45 eV [11, 12] is optimal for the maximum harvesting of the visible light in a single junction, theoretically providing over 30% of PCE as the Schockley–Quisser limit [6, 13]. Despite such an optimal bandgap, the PCE reached a record of only 4.87% in the bulk heterojunction of Bi_2S_3 nanocrystals and PbS quantum dots [14] and 1.33% in Bi_2S_3/CuI [15], ~1% in Bi_2S_3/P3HT [16], 0.36% in Bi_2S_3/BiOI [17], and 0.1–0.4% in Bi_2S_3/PbS [18] heterojunctions. In a single junction, PCE of Bi_2S_3-based SC has not overcome 1% [10]. Also, Bi_2S_3 was investigated for the role of the counter electrode material and sensitizer in Pt-free DSSC [19].

The reported experimental bandgap of crystalline Sb_2S_3 typically falls in the range of 1.72–2.24 eV [20], making it a promising absorber material for single-junction SC and as a top cell in tandem architectures. The record efficiency of single junction Sb_2S_3-based SC was reported as 7.5%, employing FTO/mp-TiO_2/Sb_2S_3/PCPDTBT/Au configuration [21]. Further, it was improved to 8.0% in FTO/CdS/Sb_2S_3/Spiro/Au configuration [22] and 8.32% by adding the perovskite layer for better charge transport and extraction in Sb_2S_3-based parallel planar heterojunction SC [23]. A recent study has also explored compositional engineering approaches to further optimise Sb_2S_3-based SC performance [24]. The best efforts in this way were reported in the alloys (solid solutions) of isostructural Sb_2S_3 and Sb_2Se_3, $Sb_2(S_{1-x}Se_x)_3$, which reached the record PCE among pseudo-1D chalcogenides, namely 10.67% [25] and 10.75% [26]. In this regard, it is intriguing to explore other alloys of isostructural pseudo-1D chalcogenides, e.g. $(Sb_xBi_{(1-x)})_2Se_3$ [27] and $(Sb_xBi_{(1-x)})_2S_3$ (studied here). Besides absorber role in SCs, Sb_2S_3 was reported as a novel material for the back surface field layer in MoS_2/Sb_2S_3/$Cu_2ZnSn_{1-x}Ge_xS_4$/CdS/ZnO/ITO solar cell structure [28], electron transport layer material for $CsPbI_2Br$ perovskite SC [29], an interlayer (in blend with PbS nanoparticles) between $CsPbI_2Br$ and the Carbon electrode for efficient hole extraction [30].

Despite all the advantages of pseudo-1D chalcogenides, the performance of Sb and Bi chalcogenide SC lags behind CdTe, CIGS and CZTS SC performances. One of the mainly assumed reasons is the point defects that may be present in the Ch in a wide variety due to their orthorhombic ribbon-like structure. The first principles study on Sb_2S_3 concluded that the dominant acceptor defects (V_{Sb}, Sb_S, and S_{Sb}) and donor defect (V_S) in intrinsic Sb_2S_3 have similar formation energies. This results in the Fermi level pinning near the middle of the band gap [20]. It may be the reason for experimentally observed high resistivity values ($\sim 10^8$ Ohm·cm), low photoluminescence (PL) (thus, the high extent of the non-radiative recombination), and PCE losses in undoped Sb_2S_3 thin films [31]. Interestingly, a sulphur treatment was noticed to enhance the PCE of the Sb_2S_3 SC. The detailed electronic structure and defect calculations suggested that the device performance can be improved by controlling S content or environment during film deposition or post-deposition sulphurisation. The passivation of the Sb_2S_3 defects and improvement in crystallinity led to an enhanced PCE (6.31%) in the *in situ* sulphurised device, outperforming the control device (PCE of 5.46%) [32]. Thioacetamide treatment was found to be instrumental in boosting the V_{OC} and PCE values from 0.57 V and 5.5% (in the control device) to 0.65 V and 7.5% (in the champion device), respectively [21]. In another study, PCE was boosted from 5.0% to 5.8% upon post-annealing sulphurisation of Sb_2S_3 solar cell. At the same time, V_{OC} reached 0.71 V [33], comparable to the highest value V_{OC} of 0.726 V in a solution-processed Sb_2S_3 solar cell [34].

Regarding Bi_2S_3, the first-principle calculations showed that all types of defects, namely the vacancies, antisites, and interstitials, can have high concentrations. Unexpectedly, most of these intrinsic defects, including even the S interstitial, act as donors, contributing to the observed n-type conductivity in Bi_2S_3 and

making it difficult to achieve a high p-type conductivity. Interestingly, under the Bi-rich and S-poor conditions (corresponding to the thermal evaporation methods' conditions), the neutral sulphur vacancy (V_S) has the lowest formation energy [11]. In contrast to Sb_2S_3, sulphur vacancies contribute to the high electrical conductivity in Bi_2S_3 (10^{-4} Ω^{-1} cm^{-1}) [35].

However, a direct correlation between experimental and theoretical defect characterisation is still missing. Also, the data on reported band edges for crystalline Bi- and Sb-chalcogenides do not agree [9, 36]. The standard methods for characterising defects' microstructure include PL to estimate non-radiative and radiative losses and identify the transition energy levels. Admittance spectroscopy (AS) and deep-level transient spectroscopy (DLTS) methods are devoted to the characterisation of the defect states in thin films at the atomic level. These techniques can provide details about the defects, such as the energy distribution of corresponding defect states, their concentration, capture cross-section, and localisation in the film. The AS measurements are mainly used to analyse shallow defect levels, while DLTS measurements can characterise deeper defect levels (greater than 0.1 eV from the band edges) [37].

Energy-resolved electrochemical impedance spectroscopy (ER-EIS) [38–40] enables the characterisation of the electronic density of states (DOS) in a wide range of energy from −8.0 eV to −2.0 eV. At the same time, information can be obtained about the band edges and defect states in the bandgap [41]. In addition to distinguishing between shallow and deep trap states, their concentration can be determined by integrating the DOS spectrum inside the bandgap [42]. Moreover, ER-EIS is a technique that does not require a vacuum and elaborate sample and experiment setup preparation. ER-EIS have been successfully applied to the analysis of various charge transfer layers [43, 44] and the polymer absorbers in organic photovoltaics [40, 45]. However, there is a lack of reports on the characterisation of DOS in chalcogenides either by ER-EIS or other experimental techniques.

In this paper, for the first time, we report the experimental DOS obtained by the ER-EIS method for the Bi- and Sb-chalcogenides and their alloys. By comparing the experimental DOS to the calculated one by density functional theory (DFT), we identify the dominant defect present in Bi- and Sb-chalcogenides fabricated by thermal evaporation techniques. Further, we explore ternary $(Sb_xBi_{(1-x)})_2S_3$ alloys of different Bi:Sb atomic ratios to fine-tune (i) band edge positions and (ii) intrabandgap defect states for Chs' photovoltaic applications and beyond. Moreover, we explain the discrepancy in the reported values of ionisation potentials and the bandgaps of Bi- and Sb-chalcogenides.

2. Methods

2.1. Materials and fabrication procedure

The samples of Bi_2S_3, Sb_2S_3 and $(Sb_xBi_{(1-x)})_2S_3$ were prepared in the form of thin films by close-space sublimation (CSS) method from the Sb_2S_3 and Bi_2S_3 precursors (ThermoElectric, 5 N purity). The deposition was made on the FTO on glass (Sigma Aldrich, surface resistivity $\sim 7\ \Omega\ sq^{-1}$) precleaned substrate. The thickness of the films was determined to be approximately 500 nm using the Veeco Dektak 150 surface profiler. The CSS parameters for pristine Bi_2S_3 and Sb_2S_3 were selected based on the deposition conditions described previously [10, 46]. The CSS deposition conditions for $(Sb_xBi_{(1-x)})_2S_3$ thin films were interpolated from the conditions for the pristine Bi_2S_3 and Sb_2S_3 films.

2.2. Characterisation techniques

2.2.1. Structure and composition characterisation

The composition and structure of the films were determined by x-ray diffraction and XRD (see figure S1(a) in SI). XRD data were acquired using a Rigaku Ultima IV diffractometer, utilising Cu Kα radiation ($\lambda = 1.54$ Å, 40 kV, 40 mA), and processed with PDXL2 software.

Both Bi_2S_3 and Sb_2S_3 crystallise in orthorhombic unit cells with the Pnma space group, which leads to similar characteristic XRD patterns which are close to the corresponding references from the XRD database, 01–074-9437 for Bi_2S_3 and 01–083-7414 for Sb_2S_3 (figure S1(a)). XRD lattice parameters of Bi_2S_3 and Sb_2S_3 correspond to the ones reported before, namely $a = 11.24$–11.33 Å, $b = 3.98$ Å, and $c = 11.12$–11.15 Å for Bi_2S_3; and $a = 11.24$–11.33 Å, $b = 3.83$ Å, and $c = 11.12$–11.23 Å for Sb_2S_3.

The designed relative atomic proportions of Bi:Sb in $(Sb_xBi_{(1-x)})_2S_3$ thin films were verified by energy dispersive x-ray spectroscopy, EDX, see figure S1(b). EDX was part of a Zeiss HR-SEM MERLIN with a GEMINI II column.

2.2.2. Optoelectronic properties characterisation

Scanning kelvin probe (SKP) (KP Technology, UK) method was used to measure contact potential difference (CPD). The CPD data were recalculated to the work function (WF), or Fermi level ($-E_F$) if the vacuum level

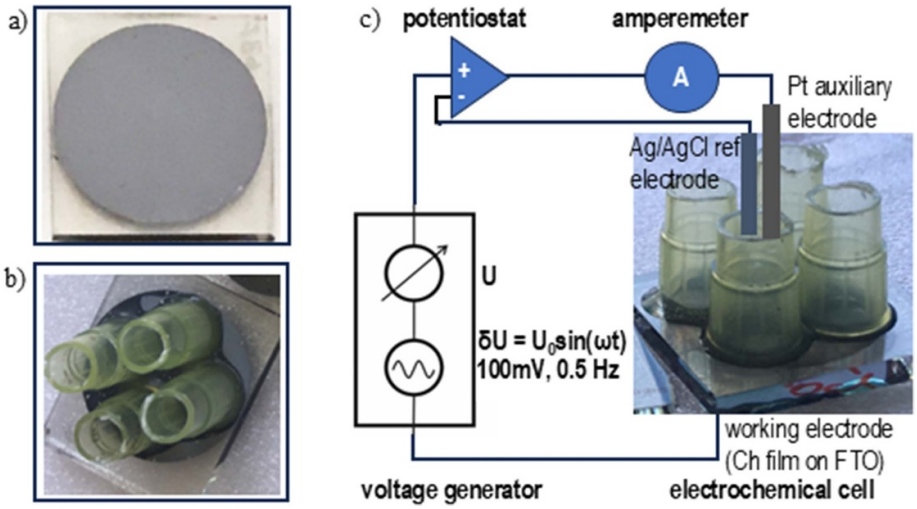

Figure 1. (a) Representative photo of the Ch film on FTO. (b) Microcells on Ch film for ER-EIS measurements. (c) ER-EIS measurement scheme.

is set to 0, values using the equation:$WF_{sample} = \left(CPD_{sample} - CPD_{ref}\right) \times 10^{-3} + WF_{ref}$. As the WF reference ($WF_{ref}$), an Au reference sample from KP Technology was used. SKP measurements were done in a glove box under ambient air conditions and a dark environment using a grounded steel probe tip of 2 mm. The WF was measured for 1 min (50 data points) at two different locations on the samples to obtain representative information and statistics.

ER-EIS experiments were performed on chalcogenide thin films shown in figure 1(a) with glued plastic cones (microcells) of about 200 ml volume on top of the films (figure 1(b)) with a potentiostat used in a conventional three-electrode configuration (figure 1(c)). The Ch film on the FTO substrate acted as the working electrode. Ag/AgCl and Pt wires were used as reference and auxiliary electrodes. To prevent electrolyte degradation due to the presence of oxygen and moisture from the air and to achieve a wide electrochemical window, measurements were performed in a glove box with a protective N_2 atmosphere (oxygen and moisture below 20 ppm and 2 ppm, respectively). A solution of tetrabutylammonium hexafluorophosphate (TBAPF6) in acetonitrile with a concentration of 0.1 M (6×1019 ions cm^{-3}) was employed as the electrolyte. The electrolyte solution can cover a voltage (energy) window of 6 V (6 eV) with respect to the Ag/AgCl reference electrode (vacuum level) and this range is sufficient to map the whole band gaps of chalcogenides. Impedance was measured using an impedance/gain-phase analyser (Solartron Analytical, model 1260) at a frequency (ω) of 0.5 Hz with an rms AC voltage of 100 mV and the bias voltage was swept with the rate of 10 mV s^{-1}. The total ER-EIS spectrum is obtained from two separate scans, each measured in new microcells to eliminate irreversible degradation of both the electrolyte and the layers under investigation. One scan started from zero to positive potentials (mapping the valence band region) and the other to negative potentials (mapping the conductance band region).

The accuracy of ER-EIS data depends on the accuracy of the AC and DC voltages applied and the measured impedance. The energy determination error is given by the setting of the surface potential of the semiconductor, which is affected by the electrolyte resistance and the amplitude of dU. The three-electrode cell eliminates electrolyte resistance and thus the energy uncertainty of ± 50 meV is determined only by dU. The error in the DOS determination given by the bridge impedance analyser used provides a measurement accuracy of 5% [38].

The directly measured value in the ER-EIS technique is the complex impedance. Its real part is extracted, and in the conditions of measurements in the medium frequency zone (0.5 Hz) the R_{CT} charge transfer resistance dominates. The R_{CT} is related to DOS in the following way:

$$\left[R_{CT}\left(E_F\right)\right]^{-1} = e^2 S\left[A\right] g\left(E_F\right) k_{et}$$

where e—elementary charge, C; S—sample working area, cm^2, with chosen microcell configuration 0.12 cm^2; [A] concentration of electrolyte, cm^{-3}; $g\ (E_F)$—DOS in $cm^{-3}eV^{-1}$; k_{et} electron transfer constant, cm^4s^{-1}.

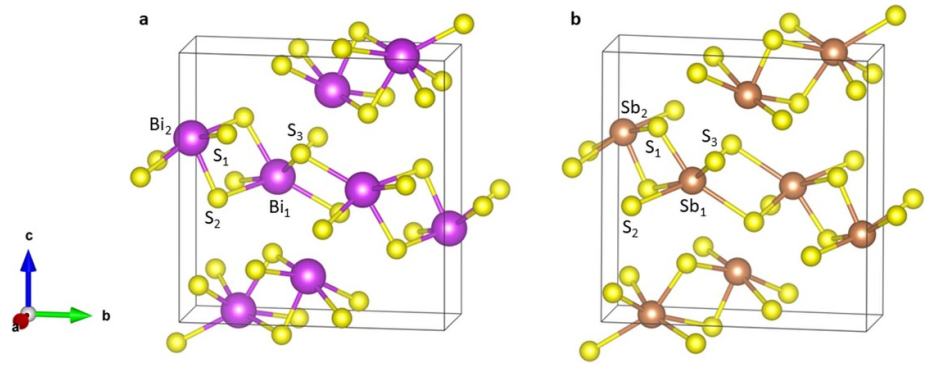

Figure 2. Unit cells employed in our DFT calculations. Labels represent atoms with slight charge differences in our Bader analysis. (a) Bi_2S_3 and (b) Sb_2S_3. Purple, brown and yellow represent bismuth, antimonium and sulphur atoms, respectively.

2.3. First-principles calculations

Ab initio calculations based on DFT [47] were performed to analyse the physicochemical properties of bulk chalcogenide materials. We performed these calculations with the VASP code [48] by following the PBEsol functional [49], which is the revised version for solids of the generalised gradient approximation to the exchange-correlation energy. Given the importance of van der Waals interactions in these materials, long-range interactions are not negligible, thus, geometry optimisations included van der Waals corrections [50]. Quantum relativistic effects on the electronic bands were taken into consideration (i.e. spin–orbit coupling corrections) for the optoelectronic calculations along with hybrid functionals, i.e. HSE06 + SOC [51, 52].

The projector augmented-wave method was used to represent the ionic cores [53, 54]. For each element, the following electrons were considered as valence: Bi s^2p^3, Sb s^2p^3, S s^2p^4. Wave functions were represented in a plane-wave basis, typically truncated at 350 eV. In the geometry relaxations, a tolerance of 0.005 eV $Å^{-1}$ was imposed in the atomic forces. For each compound, a primitive cell with 20 atoms was selected in the Brillouin zone, which was sampled with a $7 \times 2 \times 2$ Γ -centred mesh (in reciprocal space). By using these parameters, the resulting zero temperature energies were converged to within 1 meV per formula unit.

Both calculated structures converge into Pnma symmetry (see figure 2) with lattice parameters for Bi_2S_3 $a = 11.031$ Å, $b = 3.942$ Å, $c = 10.866$ Å, and for Sb_2S_3 $a = 11.033$ Å, $b = 3.815$ Å, $c = 10.818$ Å. Calculated crystal data corresponds to the experimental one obtained by XRD.

To estimate of the electronic DOS under the existence of point defects, we again used the HSE06 + SOC functional on a $2 \times 1 \times 1$ supercell. A sulphur vacancy (V_{S3}) was generated on that supercell for Sb_2S_3/Bi_2S_3 based on the results reported elsewhere [12]. The mean energy of the defect, E_D was calculated as $E_D = \int (\text{PDOS} \cdot \text{energy})\, d\text{energy} / \int \text{PDOS}\, d\text{energy}$, where PDOS is the projected DOS.

3. Results and discussion

3.1. DOS of Bi_2S_3 and Sb_2S_3 measured by ER-EIS

Firstly, DOS characterisation and interpretation were performed for the pristine Bi_2S_3 and Sb_2S_3. The band edge energies (from UPS and iPES), bandgap values (by UV–Vis), and the calculated DOS (by DFT) of these materials are well-known and can serve as a guide and reference for our characterisation. However, these data are not consistent. The minimum (prospective bandgap) and maximum intensities of the DOS vary by three orders of magnitude. Therefore, it is convenient to have an overview of the DOS in the logarithm scale shown in figures 3(a) and (b). If we consider the most intense and steepest bands in the chalcogenides at ∼−7 eV and −3 eV as the band edges, then the bandgap value obtained is ∼4 eV, which is more than twice as much compared to the data reported for Bi_2S_3 of 1.20–1.45 eV [11] and Sb_2S_3 of 1.72–2.24 eV [20]. Moreover, the most intense and steepest valence band at around −7 eV for both chalcogenides is too deep to be attributed to the VBM of the lone-electron pair chalcogenides, with a characteristic VBM feature at ∼5 eV to the vacuum level [55]. To visualise the less intense bands and fit them with mathematical functions, the DOS is presented on a linear scale in figures 3(c) and (d) with a subsequent magnification of the region adjacent to the bandgap in figures 3(e) and (f). Two types of DOS features can be distinguished. The bands labelled 1 and 2 in figures 3(a), (b) and (e), (f) are broad, square-root shaped, and not an order of magnitude higher than the bottom of the bandgap. The fitting of the 1 and 2 bands is presented in figures S2 (a)–(f). The RMS of the square root fitting is not greater than 0.11 a.u. This fit and its high accuracy support the correct assignment of features 1 and 2 to the band edges since the band edges of semiconductors exhibit a square

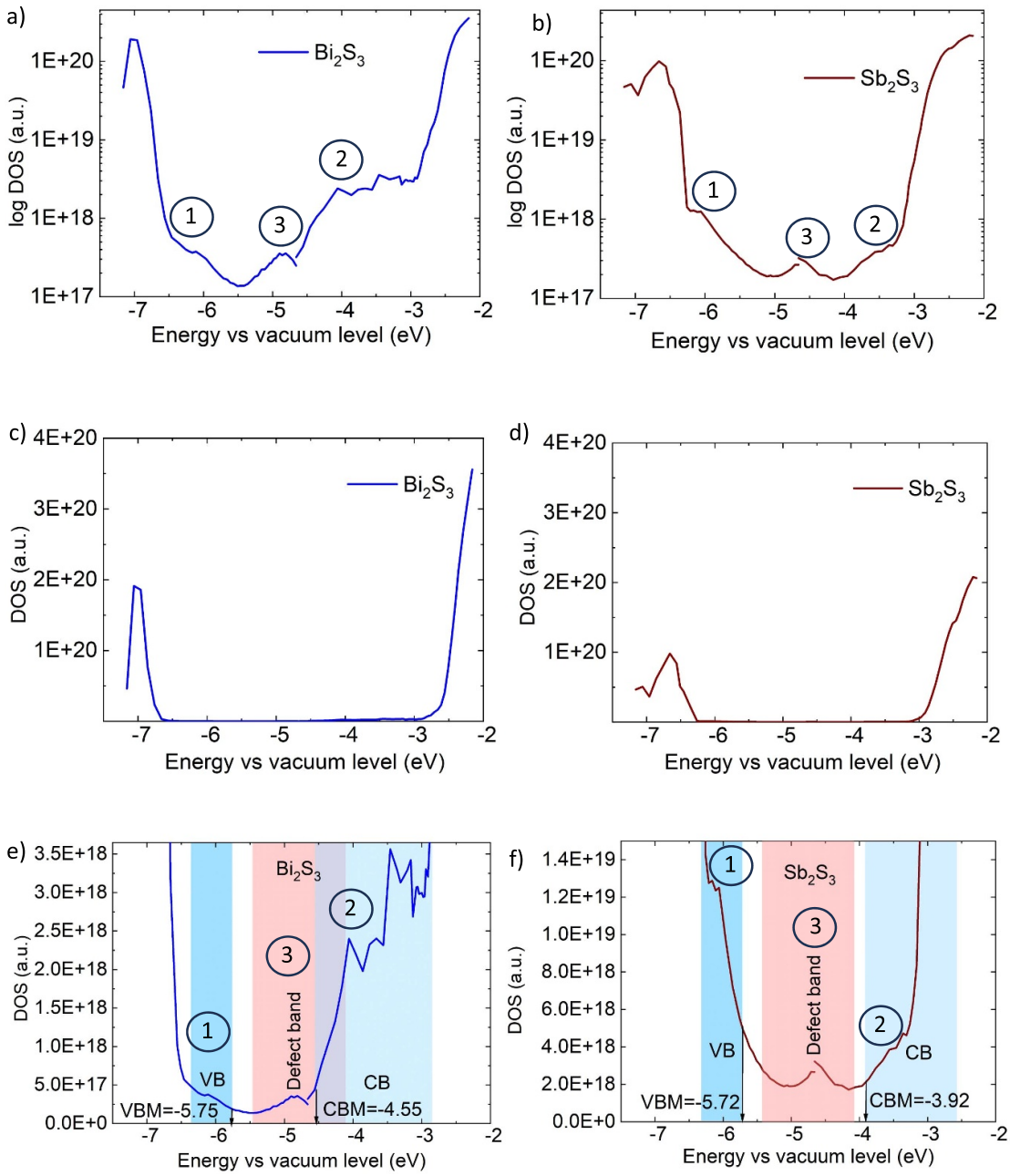

Figure 3. DOS measured by ER-EIS presented in log scale (a), (b) for the DOS features overview and in the linear scale with different magnifications (c), (d) and (e), (f) to zoom in on the possible bandgap features of pristine Bi_2S_3 and Sb_2S_3. VB—valence band, CB—conduction band.

Table 1. VBM, CBM, and bandgap (E_g) values from a square-root fit of the band edges and defect state positions (E_D) from a Gaussian fit of the defect states.

	VBM (eV)	VBM (err)	CBM (eV)	CBM (err)	*E*g (eV)	*E*g (err)	E_D (eV)	E_D (err)
Bi_2S_3	−5.75	0.09	−4.55	0.11	1.20	0.14	−4.84	0.07
Sb_2S_3	−5.72	0.08	−3.92	0.06	1.80	0.10	−4.61	0.07

root dependence [56]. The feature labelled as 3 in figures 3(a), (b) and (e), (f) has a Gaussian shape (figures S2 (g), (h) in SI) and might be related to a band of defect states, as suggested in the theoretical papers on deep defect distribution models [57–60].

The fitted curves can be seen in figure S2, and the fitting parameters of the band edges and band positions of the possible defect states are presented in table 1.

The presented values of the VBM for Bi_2S_3–5.75 eV vs the vacuum level agree well with the previously reported VBM values of chalcogenide by XPS [10]. For Sb_2S_3, the VBM of −5.72 eV vs the vacuum level is

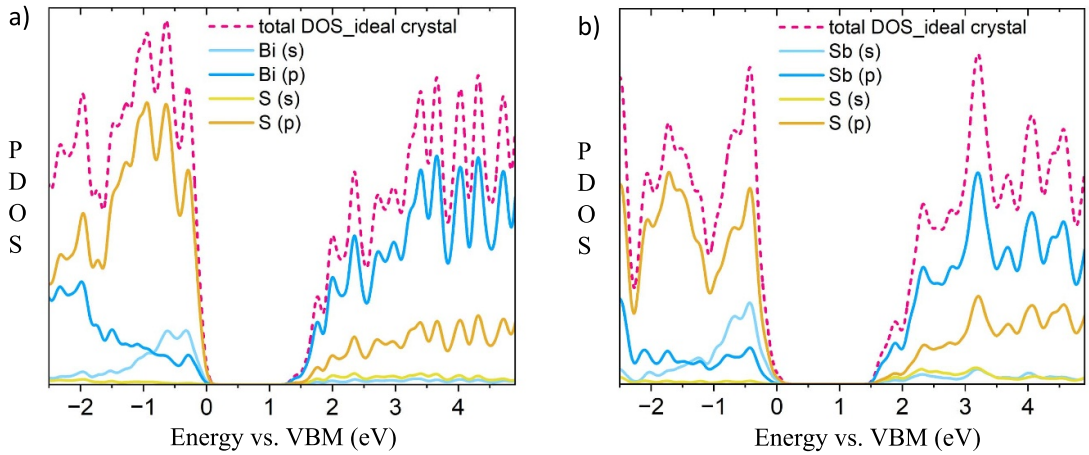

Figure 4. DOS by DFT of the ideal crystal structure of (a) Bi_2S_3 and (b) Sb_2S_3. VBM is set to 0 eV.

shifted 0.6 eV deeper from the vacuum level compared to the value measured by XPS [9]. It is worth noting that the low conductivity of Sb_2S_3 can affect the XPS measurements, and the deeper VBM in Bi_2S_3 compared to Sb_2S_3 found in our experiment was also theoretically predicted [61].

The CBM of Sb_2S_3 (−3.92 eV) is closer to the vacuum level than the CBM of Bi_2S_3 (−4.55 eV). With similar VBM positions in the chalcogenides, the bandgap of Sb_2S_3 is wider (1.80 eV) compared to Bi_2S_3 (1.20 eV). The bandgap values are in perfect agreement with previously reported data.

The Gaussian peaks at −4.84 eV in Bi_2S_3 and −4.61 eV in Sb_2S_3 can be associated with bands of defect states [57–60]. The areas under the defect peaks correspond to a defect concentration of 1.12×10^{18} cm^{-3} in Bi_2S_3 (shallow defect states) and 3.46×10^{17} cm^{-3} in Sb_2S_3 (deep defect states), which can be correlated with the free charge concentration in Bi_2S_3 and the trap level concentration in Sb_2S_3. We performed the DFT calculations of the DOS of Bi- and Sb-chalcogenides to further confirm the band assignment to the defects and identify the defect's nature.

3.2. DOS of Bi_2S_3 and Sb_2S_3 by DFT calculations

3.2.1. Ideal crystal structure

Firstly, the projected (PDOS) and total DOS were calculated for the ideal (defectless) crystal structure of pristine Bi_2S_3 and Sb_2S_3 to identify the atomic orbital contribution to the electronic DOS (figure 4).

Figure 4 shows that the S 3p orbitals dominate the lower part of the valence band. Bi and Sb ns^2 orbitals contribute to the valence band edge. The conduction band is composed principally of the Ch 6p orbitals. Thus, the CBM position will be significantly different in the Bi_2S_3 and Sb_2S_3 materials, while the VBM position is expected to be similar, which agrees with the ER-EIS results. Noteworthy, the dominant sulphur band shape in the valence band region is quite different for the compounds. Bader's analysis revealed that Bi1 atoms in the unit cell likely share fewer electrons with their coordination environment compared to Sb1, namely Bi1 shares ∼1.5 e^- and Sb1 ∼2.8 e^- (while Bi2 and Sb2 share a similar number of electrons ∼2.0 e^-). It might affect the electronic shape of the DOS of S in the valence band region. Noteworthy, there are no intrabandgap bands in the ideal crystal structure of the materials as expected.

Moreover, the DFT electronic band structure analysis (figure S3) revealed the indirect bandgap for Bi_2S_3 of 1.33 eV (in the experimental bandgap range [11]) and direct bandgap for Sb_2S_3 of 1.45 eV (it is below the experimental bandgap range of 1.72–2.24 eV [20] possibly due to DFT limitations [62, 63]). Noteworthy, the difference between calculated direct (1.45 eV) and indirect (1.48 eV) bandgaps in Sb_2S_3 is insignificant, as was reported elsewhere [36].

3.2.2. Introduction of the defects in Bi_2S_3 and Sb_2S_3 crystal structures

To reproduce the experimental DOS spectra with the intrabandgap bands, we introduced the defects in the ideal crystal structures of Bi_2S_3 and Sb_2S_3. As discussed earlier, due to the orthorhombic crystal structure of Ch, various point defects can be introduced into the Ch cell. There are two non-equivalent Me atomic sites (Me1 and Me2 in figure 2) and three non-equivalent S atomic sites (S1, S2, and S3 in figure 2). Namely, there are five possible vacancy sites and five possible antisite sites in intrinsic Me_2S_3. These include two Me vacancies (V_{Me1} and V_{Me2}), three S vacancies (V_{S1}, V_{S2}, and V_{S3}), two S antisites (S_{Sb1} and S_{Sb2}), and three Me antisites (Me_{S1}, Me_{S2}, and Me_{S3}). Because Me_2S_3 has two different elements, Me and S, it has two

Table 2. VBM by ER-EIS, E_F by kelvin probe, and the energy distance between VBM onset and E_F.

Sample	VBM (eV)	E_F (eV)	E_F–VBM (eV)
Bi_2S_3	-5.75 ± 0.09	-4.83 ± 0.02	0.92 ± 0.09
Sb_2S_3	-5.72 ± 0.08	-4.77 ± 0.04	0.95 ± 0.09

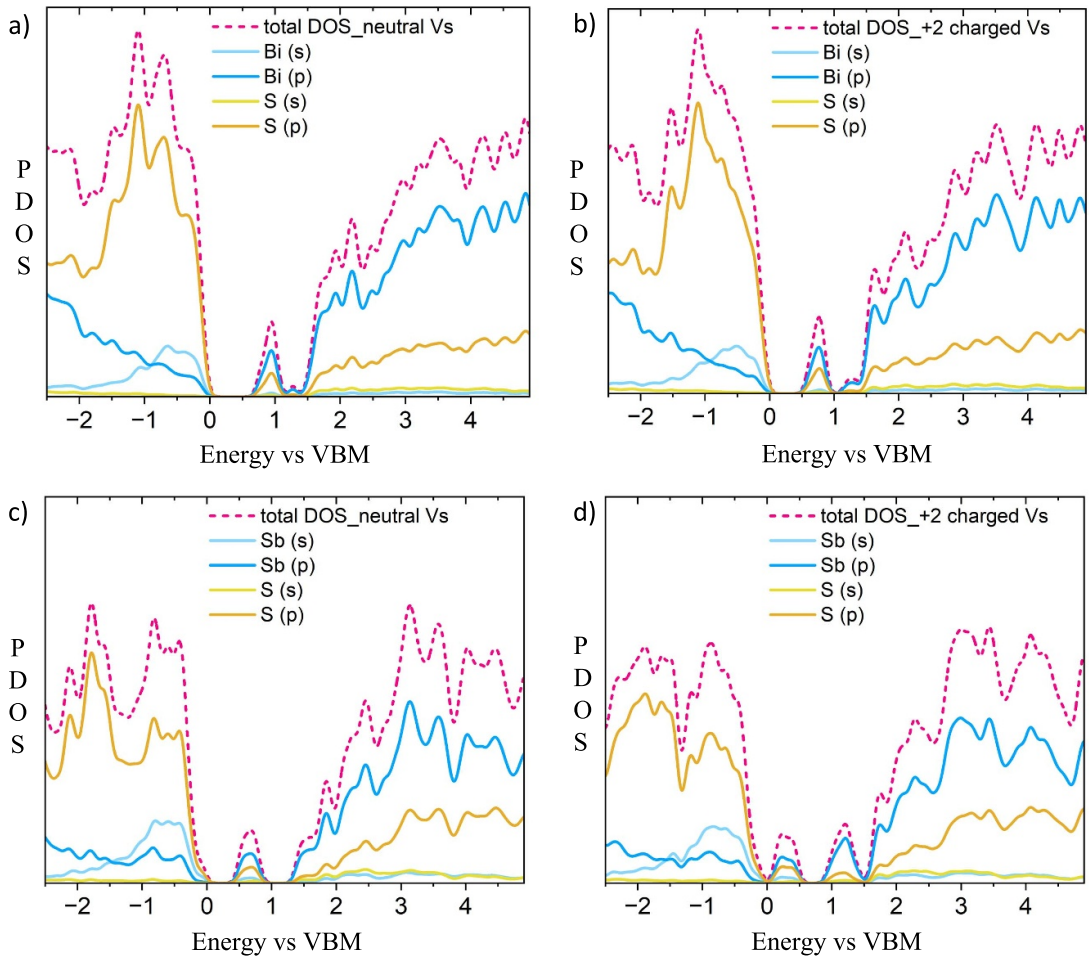

Figure 5. DOS by DFT of crystal structure with introduced neutral and charged Vs of Bi_2S_3 (a), (b) and Sb_2S_3 (c), (d). VBM is set to 0 eV. All numerical data on mean defects' energy (E_D) vs VBM from DFT calculations and ER-EIS experiments are combined in table S1.

different types of interstitials, Me_i and S_i [20]. To facilitate and decrease the number of modelled structures with defects, we performed kelvin probe characterisation of the Fermi level (E_F) of the materials to obtain the energetic distance between VBM (measured by ER-EIS) and E_F (table 2).

This E_F–VBM distance can determine the point defect in Ch with the least formation energy using the defect formation energy diagrams, which show the dependence of the defect formation energy on the position of the E_F relative to VBM (i.e. E_F–VBM) calculated and presented in [11] for Bi_2S_3 and [20] for Sb_2S_3. Noteworthy, the diagrams of only Me-rich conditions were considered as the closest to the CSS ones. From the diagrams, it appeared that the defect with the lowest formation energy at the defined E_F–VBM of Bi_2S_3 and Sb_2S_3 (table 2) is sulphur vacancy (V_S).

DOS calculations by DFT with neutral and charged V_S are shown in figures 5(a) and (b) for Bi_2S_3 and figures 5(c) and (d) for Sb_2S_3. All three different sulphur vacancies (V_{S1}, V_{S2}, and V_{S3}) introduce the same electronic state distribution in DOS spectra in our calculations. Also, Bader's analysis showed no remarkable difference among sulphur atoms. We considered V_{S2} to be the representative sulphur vacancy for Bi_2S_3 and V_{S3} to be the representative one for Sb_2S_3 and labelled any sulphur vacancy as V_S further in the text.

Calculated DOS with the neutral V_S reproduce the experimental DOS spectra of Bi_2S_3 in the following features, namely: (i) Defect band merges with the conduction band—the reason for n-type conductivity of Bi_2S_3; (ii) Energy distance between defect's mean energy and VBM is 0.92 eV for neutral V_S in DFT DOS and 0.91 eV in ER-EIS DOS.

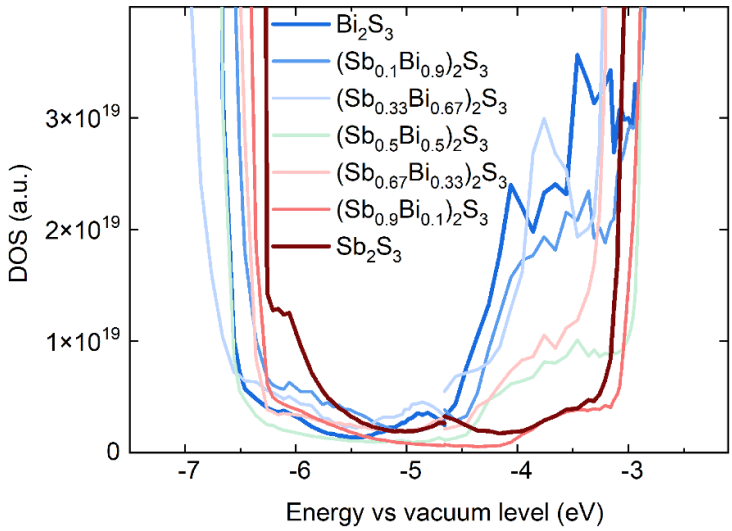

Figure 6. The set of DOS measured by ER-EIS to visualise trends in band edge positions and defect band transformation upon Sb incorporation into Bi_2S_3. Individual DOS plots of each alloy with appropriate fits can be found in the SI.

In Sb_2S_3, defects represent deep defects since their DOS band does not merge with the valence and conduction bands in both DFT and ER-EIS DOS. The distance between the defect's mean energy and VBM is 0.66 eV for neutral V_S in DFT DOS and 1.11 eV in ER-EIS DOS. Such a difference most probably originates from the different onsets of calculated and experimental VBMs since the structural disorder was not introduced in the calculated structures, while it could affect the determination of VBM onset in the experimental spectra (figure S2). Despite the difference in calculated and experimental E_D energies in Sb_2S_3, the dominance of V_S in Sb_2S_3 suggested in this work agrees with [64].

3.3. DOS of $(Sb_xBi_{(1-x)})_2S_3$ alloys measured by ER-EIS

DOS spectra of Bi_2S_3 and Sb_2S_3 are quite distinct, as shown in figure 3. This fact brought us to the following questions: (i) Is there any trend in DOS transformation (band edges, defects) while subsequently 'substituting' Bi by Sb in $(Sb_xBi_{(1-x)})_2S_3$ alloys, or does the transformation happen abruptly from one particular alloy to the other? (ii) What is the minimum quantity of Bi in $(Sb_xBi_{(1-x)})_2S_3$ required to eliminate the midgap defects in Sb_2S_3?

To answer these questions ER-EIS investigation of the alloys was performed, and the results are presented in figure 6 (merged DOS spectra) and figure S4 (separated DOS spectra). The most evident change occurs in the CBM region. Namely, CBM position shifts gradually from −4.55 eV (Bi_2S_3 and $x = 0.1$ and 0.33 $(Sb_xBi_{(1-x)})_2S_3$ alloys) to ∼ −4.2 eV ($x = 0.5$ and 0.67 $(Sb_xBi_{(1-x)})_2S_3$ alloys) and −3.92 eV in $(Sb_{0.9}Bi_{0.1})_2S_3$ alloy and Sb_2S_3. The CBM intensity experiences a gradual drop from ∼2.0×10^{19} a.u. (Bi_2S_3 and $x = 0.1$ and 0.33 $(Sb_xBi_{(1-x)})_2S_3$ alloys) to ∼ 1.0×10^{19} ($x = 0.5$ and 0.67 $(Sb_xBi_{(1-x)})_2S_3$ alloys) and 0.5×10^{19} ($(Sb_{0.9}Bi_{0.1})_2S_3$ alloy and Sb_2S_3). In contrast to the CBM intensity trend, the VBM intensity remains as low as ∼0.5×10^{19} a.u. in Bi_2S_3 and all the alloys, and only in Sb_2S_3 does it surpass ∼1.0×10^{19} a.u. The VBM shift to the vacuum level with the Sb content increase is insignificant (below the error of VBM estimation). DFT calculations in figures 5(a) and (c) show it is Me orbitals that are responsible for CBM formation. Thus, the CBM region is expected to experience the largest transformation during the Bi:Sb ratio change in the alloys from a theoretical perspective that aligns with ER-EIS results.

Importantly, the 1:9 ratio of Bi:Sb in $(Sb_{0.9}Bi_{0.1})_2S_3$ is already enough to eliminate the midgap defect states while keeping the band edges unchanged compared to those of Sb_2S_3. It provides a strategy to control the defect ratio without changing the Sb_2S_3 crystal structure, which is crucial for optimising electrical conductivity on the one hand and non-radiative recombination on the other hand.

4. Conclusions

The above analyses show that ER-EIS is a practical, simple method to investigate the electronic structure of chalcogenides straightforwardly. The careful fitting of ER-EIS spectra makes it possible to distinguish between band edges and the bands of the defects in the Bi- and Sb-chalcogenides. Specifically, (i) VBM position was determined to be at −5.75 eV for Bi_2S_3 and −5.72 eV for Sb_2S_3; consequently, (ii) CBM position is at −4.55 eV for Bi_2S_3 and −3.92 eV for Sb_2S_3; and (iii) the transport bandgap is 1.20 eV and

1.80 eV for Bi_2S_3 and Sb_2S_3, respectively. The Gaussian-like peak in DOS spectra at −4.84 eV in Bi_2S_3 and −4.61 eV in Sb_2S_3 is associated with the band of the defect states. The area under this peak corresponds to a defect concentration of 1.12×10^{18} cm^{-3} in Bi_2S_3 (shallow defect) and 3.46×10^{17} cm^{-3} in Sb_2S_3 (deep defect) that can be correlated with the free charge concentration in Bi_2S_3 and the concentration of trap levels in Sb_2S_3. By comparing DFT-calculated and ER-EIS-measured DOS spectra, it is possible to reveal the nature of the point defects in the materials. The sulphur vacancy is the dominant defect in both Bi_2S_3 and Sb_2S_3 fabricated by thermal evaporation techniques, leading to shallow defect states below the CBM in Bi_2S_3 and deep defect states in Sb_2S_3. We also showed that already in $(Sb_{0.9}Bi_{0.1})_2S_3$ alloys with the 1:9 Bi:Sb ratio, the deep defects in Sb_2S_3 are removed while VBM and CBM are close to the ones in Sb_2S_3. This may provide a novel strategy for healing the deep defects, thus possibly mitigating non-radiative recombination and tuning electrical conductivity in Sb_2S_3, which is crucial for boosting PV performance. The impact on Sb_2S_3 SC performance improvement and the actual mechanism of defect passivation, by Bi incorporation in Sb_2S_3, is a matter of further research.

Data availability statement

The data that support the findings of this study are openly available at the following URL/DOI: https://zenodo.org/records/14051298 [65].

Acknowledgment

This research was funded by MSCA PF action, project BOOSTPV, Grant No. 101109054, the Estonian Research Council project PSG689 'Bismuth Chalcogenide Thin-Film Disruptive Green Solar Technology for Next Generation Photovoltaics', the Estonian Ministry of Education and Research project TK210; TK210U8 'Center of Excellence in Sustainable Green Hydrogen and Energy Technologies', and the work was supported by EU Horizon 2020 project 952509-5GSOLAR.

V.N. acknowledges the support of the Scientific Grant Agency VEGA under Project No. 2/0165/22.

CC acknowledges support from the Spanish Ministry of Science, Innovation and Universities under the fellowship RYC2018-024947-I and grants PID2020-112975GB-I00 and TED2021-130265B-C22. CL acknowledges support from the Spanish Ministry of Science, Innovation and Universities under an FPU grant. The authors also thankfully acknowledge technical support for the computational resources at MareNostrum4 provided by the Barcelona Supercomputing Center (FI-2024-1-0025, FI-2024-2-0006, FI-2024-1-0005, FI-2024-2-0003).

BR and JK thank for the support of the MEYS project No. CZ.02.01.01/00/22_008/0004617 (EcoStor) under the Operational Programme Johannes Amos Comenius.

This article is based on work from COST Action Research and International Networking on Emerging Inorganic Chalcogenides for Photovoltaics (RENEW-PV), CA21148, supported by COST (European Cooperation in Science and Technology).

DM is grateful to her coauthor Vojtech Nadazdy for his unconditional ER-EIS experimental knowledge sharing, Kostiantyn Sopiha for useful discussions on the defects in materials, Rico Meitzner for his support, PV enthusiasm and PV knowledge sharing.

Conflict of interest

The authors have no conflicts to disclose.

ORCID iDs

Daria Miliaieva https://orcid.org/0000-0001-6176-1901
Vojtech Nadazdy https://orcid.org/0000-0003-4127-5249
Cibrán López https://orcid.org/0000-0003-3949-5058
Hanieh Saeeyekta https://orcid.org/0009-0005-8365-0168
Jaroslav Kuliček https://orcid.org/0000-0002-8600-7822
Edgardo Saucedo https://orcid.org/0000-0003-2123-6162
Raitis Grzibovskis https://orcid.org/0000-0001-5863-2295
Bohuslav Rezek https://orcid.org/0000-0002-0378-4598

References

[1] Lin T-Y, Hsieh C-F, Kanai A, Yashiro T, Zeng W-J, Ma J-J, Hung S-F and Sugiyama M 2024 Radiation resistant chalcopyrite CIGS solar cells: proton damage shielding with Cs treatment and defect healing via heat-light soaking *J. Mater. Chem. A* **12** 7536–48

[2] Saparov B 2022 Next generation thin-film solar absorbers based on chalcogenides *Chem. Rev.* **122** 10575–7

[3] Wang W, Winkler M T, Gunawan O, Gokmen T, Todorov T K, Zhu Y and Mitzi D B 2014 Device characteristics of CZTSSe thin-film solar cells with 12.6% efficiency *Adv. Energy Mater.* **4** 1301465

[4] Li Y, Cui C, Wei H, Shao Z, Wu Z, Zhang S, Wang X, Pang S and Cui G 2024 Suppressing element inhomogeneity enables 14.9% efficiency CZTSSe solar cells *Adv. Mater.* **36** 2400138

[5] Kumar M, Dubey A, Adhikari N, Venkatesan S and Qiao Q 2015 Strategic review of secondary phases, defects and defect-complexes in kesterite CZTS–Se solar cells *Energy Environ. Sci.* **8** 3134–59

[6] Ganose A M, Savory C N and Scanlon D O 2016 Beyond methylammonium lead iodide: prospects for the emergent field of ns^2 containing solar absorbers *Chem. Commun.* **53** 20–44

[7] McKenna K P 2021 Self-healing of broken bonds and deep gap states in Sb_2Se_3 and Sb2S_3 *Adv. Electron. Mater.* **7** 2000908

[8] Hadke S, Huang M, Chen C, Tay Y F, Chen S, Tang J and Wong L 2022 Emerging chalcogenide thin films for solar energy harvesting devices *Chem. Rev.* **122** 10170–265

[9] Krautmann R, Spalatu N, Josepson R, Nedzinskas R, Kondrotas R, Gržibovskis R, Vembris A, Krunks M and Oja Acik I 2023 Low processing temperatures explored in Sb_2S_3 solar cells by close-spaced sublimation and analysis of bulk and interface related defects *Sol. Energy Mater. Sol. Cells* **251** 112139

[10] Koltsov M, Gopi S V, Raadik T, Krustok J, Josepson R, Gržibovskis R, Vembris A and Spalatu N 2023 Development of Bi_2S_3 thin film solar cells by close-spaced sublimation and analysis of absorber bulk defects via in-depth photoluminescence analysis *Sol. Energy Mater. Sol. Cells* **254** 112292

[11] Han D, Du M-H, Dai C-M, Sun D and Chen S 2017 Influence of defects and dopants on the photovoltaic performance of Bi_2S_3 : first-principles insights *J. Mater. Chem. A* **5** 6200–10

[12] Zhan S-Q, Wan H, Xu L, Huang W-Q, Huang G-F, Long J-P and Peng P 2014 Native vacancy defects in bismuth sulphide *Int. J. Mod. Phys. B.* **28** 1450150

[13] Shockley W and Queisser H J 1961 Detailed balance limit of efficiency of p-n junction solar cells *J. Appl. Phys.* **32** 510–9

[14] Rath A K, Bernechea M, Martinez L, de Arquer F P G, Osmond J and Konstantatos G 2012 Solution-processed inorganic bulk nano-heterojunctions and their application to solar cells *Nat. Photon.* **6** 529–34

[15] Sonar S M, Guo Z, Ibrahim M M, Mersal G A M, Tarkas H S and Ahirrao P B 2024 Study of photoelectrochemical (PEC) solar cell properties of n-type bismuth sulfide (n-Bi_2S_3)/p-type copper (I) iodide (p-CuI) heterojunction synthesized by SILAR *J. Mater. Sci. Mater. Electron.* **35** 1616

[16] Martinez L, Stavrinadis A, Higuchi S, Diedenhofen S L, Bernechea M, Tajima K and Konstantatos G 2013 Hybrid solution-processed bulk heterojunction solar cells based on bismuth sulfide nanocrystals *Phys. Chem. Chem. Phys.* **15** 5482–7

[17] Fang M, Jia H, He W, Lei Y, Zhang L and Zheng Z 2015 Construction of flexible photoelectrochemical solar cells based on ordered nanostructural BiOI/Bi_2 S_3 heterojunction films *Phys. Chem. Chem. Phys.* **17** 13531–8

[18] Moreno-García H, Nair M T S and Nair P K 2011 All-chemically deposited Bi_2S_3/PbS solar cells *Thin Solid Films* **519** 7364–8

[19] Isaqu J P, Vnekatesan R, Nagalingam R, Mayandi J and Perumal N 2022 BiS can do it all: sensitizer, counter electrode, and supercapacitor for symmetric solar cell assisted photo-supercapacitor *Int. J. Energy Res.* **46** 11065–78

[20] Cai Z, Dai C-M and Chen S 2020 Intrinsic defect limit to the electrical conductivity and a two-step p-type doping strategy for overcoming the efficiency bottleneck of Sb_2S_3-based solar cells *Sol. RRL* **4** 1900503

[21] Choi Y C, Lee D U, Noh J H, Kim E K and Seok S I 2014 Highly improved Sb_2S_3 sensitized-inorganic–organic heterojunction solar cells and quantification of traps by deep-level transient spectroscopy *Adv. Funct. Mater.* **24** 3587–92

[22] Wang S *et al* 2022 A novel multi-sulfur source collaborative chemical bath deposition technology enables 8%-efficiency Sb_2S_3 planar solar cells *Adv. Mater.* **34** 2206242

[23] Zhu L *et al* 2023 Parallel planar heterojunction strategy enables Sb_2S_3 solar cells with efficiency exceeding 8 % *Angew. Chem.* **135** e202312951

[24] López C, Caño I, Rovira D, Benítez P, Asensi J M, Jehl Z, Tamarit J-L, Saucedo E and Cazorla C 2024 Machine-learning aided first-principles prediction of earth-abundant pnictogen chalcohalide solid solutions for solar-cell devices *Adv. Funct. Mater.* **34** 2406678

[25] Ren D *et al* 2025 PO_4^{3-} tetrahedron assisted chelate engineering for 10.67%-Efficient antimony selenosulfide solar cells *Adv. Mater.* **37** 2416885

[26] Chen X, Che B, Zhao Y, Wang S, Li H, Gong J, Chen G, Chen T, Xiao X and Li J 2023 Solvent-assisted hydrothermal deposition approach for highly-efficient $Sb_2(S,Se)_3$ thin-film solar cells *Adv. Energy Mater.* **13** 2300391

[27] Caño I *et al* 2023 Challenges and improvement pathways to develop quasi-1D $(Sb_{1-x}Bi_x)_2Se_3$-based materials for optically tuneable photovoltaic applications. Towards chalcogenide narrow-bandgap devices *Sol. Energy Mater. Sol. Cells* **251** 112150

[28] Goumri-Said S, Ziane M I, Belarbi M and Kanoun M B 2024 Tuning the electronic and optical properties of $Cu_2ZnSn_1-GeS_4$ alloys for photovoltaic applications: a hybrid density functional theory and device simulation approach *Battery Energy* **n/a** e20240066

[29] Jing Y, Liu X, Xu Y, Zhang M, Li R, Wang S, Yan Z, Sun W, Wu J and Lan Z 2023 Amorphous antimony sulfide nanoparticles construct multi-contact electron transport layers for efficient carbon-based all-inorganic $CsPbI_2Br$ perovskite solar cells *Chem. Eng. J.* **455** 140871

[30] Liu F *et al* 2025 Blending of Sb_2S_3/PbS nanoparticles optimizes the $CsPbI_2Br$ perovskite/carbon electrode interface to facilitate efficient charge carrier transfer in perovskite solar cells *Chem. Eng. J.* **508** 161029

[31] Barthwal S, Kumar R and Pathak S 2022 Present status and future perspective of antimony chalcogenide (Sb_2X_3) photovoltaics *ACS Appl. Energy Mater.* **5** 6545–85

[32] Huang Y, Tang R, Xiao P, Che B, Wang Y, Gao H, Wang G, Zhu C and Chen T 2022 Efficient *in situ* sulfuration process in hydrothermally deposited Sb_2S_3 absorber layers *ACS Appl. Mater. Interfaces* **14** 54822–9

[33] Yin H, Ma L-K, Wang Y, Huang J, Yu H, Zhang J, Chow P C Y, Ma W, So S K and Yan H 2019 Donor polymer can assist electron transport in bulk heterojunction blends with small energetic offsets *Adv. Mater.* **31** 1903998

[34] Eensalu J S, Tõnsuaadu K, Oja Acik I and Krunks M 2022 Sb_2S_3 thin films by ultrasonic spray pyrolysis of antimony ethyl xanthate *Mater. Sci. Semicond. Process.* **137** 106209

[35] Mizoguchi H, Hosono H, Ueda N and Kawazoe H 1995 Preparation and electrical properties of Bi_2S_3 whiskers *J. Appl. Phys.* **78** 1376–8

[36] Yang R X, Butler K T and Walsh A 2015 Assessment of hybrid organic–inorganic antimony sulfides for earth-abundant photovoltaic applications *J. Phys. Chem. Lett.* **6** 5009–14
[37] Wang R, Qin D, Zheng S, Weng G, Hu X, Tao J, Chu J, Akiyama H and Chen S 2023 Influence of S-content ratios on the defect properties of $Sb_2(S_x, Se_{1-x})_3$ thin-film solar cells *Sol. Energy Mater. Sol. Cells* **260** 112501
[38] Nádaždy V, Schauer F and Gmucová K 2014 Energy resolved electrochemical impedance spectroscopy for electronic structure mapping in organic semiconductors *Appl. Phys. Lett.* **105** 142109
[39] Schauer F, Nádaždy V and Gmucová K 2018 Electrochemical impedance spectroscopy for study of electronic structure in disordered organic semiconductors—possibilities and limitations *J. Appl. Phys.* **123** 161590
[40] Bässler H, Kroh D, Schauer F, Nádaždy V and Köhler A 2021 Mapping the density of states distribution of organic semiconductors by employing energy resolved–electrochemical impedance spectroscopy *Adv. Funct. Mater.* **31** 2007738
[41] Toriyama M Y, Ganose A M, Dylla M, Anand S, Park J, Brod M K, Munro J M, Persson K A, Jain A and Snyder G J 2022 How to analyse a density of states *Mater. Today Electron.* **1** 100002
[42] Brunova A *et al* 2021 Structural and trap-state density enhancement in flash infrared annealed perovskite layers *Adv. Mater. Interfaces* **8** 2100355
[43] Volk S, Yazdani N, Sanusoglu E, Yarema O, Yarema M and Wood V 2018 Measuring the electronic structure of nanocrystal thin films using energy-resolved electrochemical impedance spectroscopy *J. Phys. Chem. Lett.* **9** 1384–92
[44] Din M F U *et al* 2023 Tailoring the electronic properties of the SnO_2 nanoparticle layer for n-i-p perovskite solar cells by $Ti_3C_2T_X$ MXene *Mater. Today Commun.* **36** 106700
[45] Karki A, Wetzelaer G-J A H, Reddy G N M, Nádaždy V, Seifrid M, Schauer F, Bazan G C, Chmelka B F, Blom P W M and Nguyen T-Q 2019 Unifying energetic disorder from charge transport and band bending in organic semiconductors *Adv. Funct. Mater.* **29** 1901109
[46] Krautmann R, Spalatu N, Gunder R, Abou-Ras D, Unold T, Schorr S, Krunks M and Oja Acik I 2021 Analysis of grain orientation and defects in Sb_2Se_3 solar cells fabricated by close-spaced sublimation *Sol. Energy* **225** 494–500
[47] Kohn W and Sham L J 1965 Self-consistent equations including exchange and correlation effects *Phys. Rev.* **140** A1133–8
[48] Kresse G and Furthmüller J 1996 Efficient iterative schemes for ab initio total-energy calculations using a plane-wave basis set *Phys. Rev. B* **54** 11169–86
[49] Perdew J P, Ruzsinszky A, Csonka G I, Vydrov O A, Scuseria G E, Constantin L A, Zhou X and Burke K 2008 Restoring the density-gradient expansion for exchange in solids and surfaces *Phys. Rev. Lett.* **100** 136406
[50] Grimme S, Antony J, Ehrlich S and Krieg H 2010 A consistent and accurate ab initio parametrization of density functional dispersion correction (DFT-D) for the 94 elements H-Pu *J. Chem. Phys.* **132** 154104
[51] Heyd J, Scuseria G E and Ernzerhof M 2003 Hybrid functionals based on a screened Coulomb potential *J. Chem. Phys.* **118** 8207–15
[52] Krukau A V, Vydrov O A, Izmaylov A F and Scuseria G E 2006 Influence of the exchange screening parameter on the performance of screened hybrid functionals *J. Chem. Phys.* **125** 224106
[53] Blöchl P E 1994 Projector augmented-wave method *Phys. Rev. B* **50** 17953–79
[54] Kresse G and Joubert D 1999 From ultrasoft pseudopotentials to the projector augmented-wave method *Phys. Rev. B* **59** 1758–75
[55] Whittles T J *et al* 2019 Band alignments, band gap, core levels, and valence band states in Cu_3BiS_3 for photovoltaics *ACS Appl. Mater. Interfaces* **11** 27033–47
[56] Wager J F 2017 Real- and reciprocal-space attributes of band tail states *AIP Adv.* **7** 125321
[57] Chang K-C, Dai T, Wang Z, Huang Z, Lin X and Li L 2022 The observation of Gaussian distribution and origination identification of deep defects in AlGaN/GaN MIS-HEMT *Appl. Phys. Lett.* **120** 172107
[58] Smith Z E, Aljishi S and Wagner S 1987 Equilibrium between band tails and dangling bonds in a-Si:H *J. Non-Cryst. Solids* **97–98** 775–8
[59] Jain S K, Joshi A M, Bharti D, Kirpalani C and Bansal P 2024 Effect of Gaussian defect density variations on electrical characteristics of TIPS-pentacene-based OTFT *Electr. Eng.* **107** 3063–74
[60] Ramanujam J and Verma A 2012 Photovoltaic properties of a-Si:H Films grown by plasma enhanced chemical vapor deposition: a review *Mater. Express* **2** 177–96
[61] Tumelero M A, Faccio R and Pasa A A 2016 Unraveling the native conduction of trichalcogenides and its ideal band alignment for new photovoltaic interfaces *J. Phys. Chem. C* **120** 1390–9
[62] Morales-García Á, Valero R and Illas F 2017 An empirical, yet practical way to predict the band gap in solids by using density functional band structure calculations *J. Phys. Chem. C* **121** 18862–6
[63] Perdew J P 1985 Density functional theory and the band gap problem *Int. J. Quantum Chem.* **28** 497–523
[64] Wang X, Kavanagh S R and Walsh A 2025 Sulfur vacancies limit the open-circuit voltage of Sb_2S_3 solar cells *ACS Energy Lett.* **10** 161–7
[65] Kuliček J, Bouzek K and Carda M 2024 Dataset of "Energy Distribution and Identification of the Defects in Bismuth and Antimony Sulphides Revealed by Energy - Resolved Electrochemical Impedance Spectroscopy" (Version 1) *Zenodo* 10.5281/zenodo.14051298